Markedly different impacts of primary emissions and secondary aerosol formations on aerosol mixing states revealed by simultaneous measurements of CCNC, V/HTDMA and SP2

Jiangchuan Tao[1,8], Biao Luo[1,8], Weiqi Xu[3], Gang Zhao[6], Hanbin Xu[5], Biao Xue[1,8], Miaomiao Zhai[1,8], Wanyun Xu[4], Huarong Zhao[7], Sanxue Ren[7], Guangsheng Zhou[7], Li Liu[2,*], Ye Kuang[1,8,*] , Yele Sun[3]

[1] Institute for Environmental and Climate Research, Jinan University, Guangzhou, Guangdong, China

[2] Key Laboratory of Regional Numerical Weather Prediction, Institute of Tropical and Marine Meteorology, China Meteorological Administration, Guangzhou, China.

[3] State Key Laboratory of Atmospheric Boundary Layer Physics and Atmospheric Chemistry, Institute of Atmospheric Physics, Chinese Academy of Sciences, Beijing, China.

[4] State Key Laboratory of Severe Weather, Key Laboratory for Atmospheric Chemistry, Institute of Atmospheric Composition, Chinese Academy of Meteorological Sciences, Beijing, China

[5] Experimental Teaching Center, Sun Yat-Sen University, Guangzhou, China

[6] State Key Joint Laboratory of Environmental Simulation and Pollution Control, International Joint Laboratory for Regional Pollution Control, Ministry of Education, College of Environmental Sciences and Engineering, Peking University, Beijing 100871, China

[7] Hebei Gucheng Agricultural Meteorology National Observation and Research Station, Chinese Academy of Meteorological Sciences, Beijing, 100081, China

[8] Guangdong-Hongkong-Macau Joint Laboratory of Collaborative Innovation for Environmental Quality, Jinan University, Guangzhou, Guangdong, China

Correspondence: Ye Kuang (kuangye@jnu.edu.cn), Li Liu (liul@gd121.cn)

25 **Abstract**

26   The aerosol mixing state is a crucial physical-chemical property that affects their optical

27 properties and cloud condensation nuclei (CCN) activity. Multiple techniques are commonly employed

28 to determine aerosol mixing states for various applications, and comparisons between these techniques

29 provide insights of the variations in aerosol chemical and physical properties. These techniques include

30 size-resolved CCN activity measurements using a system with CCN counter (CCNC) coupled with a

31 differential mobility analyzer (DMA), a Humidified/Volatility Tandem differential mobility analyzer

32 (H/V-TDMA) which measures aerosol hygroscopicity/volatility distributions, and a single particle

33 soot photometer (SP2) which directly quantifies black carbon (BC) mixing states. This study provides

34 a first time intercomparisons of aerosol mixing state parameters obtained through simultaneous

35 measurements of a DMA-CCNC, a H/VTDMA and a DMA-SP2. The impact of primary aerosols

36 emissions and secondary aerosol formations on the aerosol mixing states and intercomparison results

37 were analyzed. The results showed that differences in mixing state parameters measured by different

38 techniques varied greatly under different conditions. The V-TDMA and DMA-SP2 measurements

39 showed that the non-volatile population identified by the V-TDMA was mainly contributed by BC-

40 containing aerosols. The HTDMA and DMA-SP2 measurements indicated that a substantial proportion

41 of nearly hydrophobic aerosols were not contributed from BC-containing aerosols, but likely

42 originated from fossil fuel combustion and biomass burning emissions. Synthesized comparison results

43 between DMA-CCNC, HTDMA and DMA-SP2 measurements revealed that some of the nearly

44 hydrophobic BC-free particles were CCN-inactive under supersaturated conditions, likely from fossil

45 combustion emissions, while others were CCN-active under supersaturated conditions linked to

46 biomass burning emissions. Fossil fuel combustion-emitted BC-containing aerosols tended to be more

47 externally mixed with other aerosol compositions compared to those emitted from biomass burning

48 activities. These results highlight significant disparities in the mixing states as well as physiochemical

49 properties between aerosol originated from fossil fuel combustion and biomass burning. The formation

50 of secondary nitrate and organic aerosols exerted significant impacts on variations in aerosol mixing

51 states, generally enhancing aerosol hygroscopicity and volatility, while reducing differences in mixing

52 state parameters derived from different techniques, resulting in a reduction in aerosol heterogeneity.

53 The variations in BC-free particle number fractions showed that secondary aerosols tended to form

54 more quickly on BC-free particles than on BC-containing particles. Further comparison of mixing state

55 parameters revealed that the two resolved SOA factors in this study exhibited remarkably different

56 physical properties, indicating that they were likely formed through different pathways. These findings

57 suggest that intercomparisons among aerosol mixing states derived from different techniques can

58 provide deeper insight into aerosol physical properties and how they are impacted by secondary aerosol

59 formation, aiding the investigation of secondary aerosol formation pathways.

60

61

1 Introduction

The aerosol mixing state is a crucial physicochemical property of aerosol particles (Riemer et al., 2019), exerting a significant impact on their optical properties and cloud condensation nuclei (CCN) activity, affecting their impact on climate and the environment (Fierce et al., 2017; Riemer et al., 2019; Stevens et al., 2022). For instance, variations in the mixing state of black carbon (BC) particles can significantly alter their absorption and radiative effects (Bond et al., 2013; Lack et al., 2012; Zhao et al., 2019; Moffet et al., 2016; Matsui et al., 2018; Peng et al., 2016). Using simple internally mixing state assumptions for aerosol chemical compositions in estimating CCN number concentrations can lead to substantial overestimations (Deng et al., 2013; Farmer et al., 2015; Ren et al., 2018; Ching et al., 2017, 2019; Tao et al., 2021). The aerosol mixing state varies widely due to complex emissions and atmospheric transformations, leading to significant uncertainties in estimating the effects of aerosol based on simplified mixing state assumptions (Ervens, 2015; Wang et al., 2022; Fu et al., 2022).

The aerosol mixing state describes the mixture of aerosol chemical components within each single particle and the distribution of these particles in the aerosol population. This property can be directly measured by the single particle chemical composition techniques (Fierce et al., 2017; Riemer et al., 2019), such as single particle soot photometer (SP2) that measures refractory black carbon (rBC) mass concentrations and the mixing state of rBC with other aerosol components or single particle chemical composition measurement techniques (e.g. SP-AMS) that have been developed over recent years (Lee et al., 2019; Riemer et al., 2019 and reference therein). Alternatively, the aerosol mixing state can be inferred from indirect measurements of aerosol properties, such as size-resolved aerosol CCN activity (measured by coupling a differential mobility analyzer (DMA) and a CCN counter (CCNC)), size-resolved aerosol hygroscopicity distributions or volatility distributions (measured by a Humidified/Volatility Tandem differential mobility analyzer (H/V-TDMA)).

However, each technique yields information on aerosol mixing states based on different aerosol micro-physical properties, thus obtain aerosol mixing states that are different but linked to one another. For instance, while both CCN activity and the hygroscopic growth measurements are associated with aerosol hygroscopicity, intercomparison between CCNC and HTDMA measurements promoted investigations on aerosol hygroscopicity variations under different saturation conditions (Su et al., 2010; Juranyi et al., 2013; Lance et al., 2013; Kawana et al., 2016; Tao et al., 2020; Jiang et al., 2021).

91   Although both SP2 and VTDMA techniques depend on the evaporation of non-refractory compositions,

92   only the rBC remains in SP2 measurements, whereas the non-refractory composition evaporations

93   depend on thermodenuder temperature in VTDMA measurements. Thus, measurements of an SP2 are

94   highly correlated to those of a VTDMA at high temperatures, with their differences reflecting

95   variations in aerosol density, shape or volatility (Philippin et al., 2004; Wehner et al., 2009; Adachi et

96   al., 2018, 2019; Wang et al., 2022). HTDMA and VTDMA can be applied in combination to study the

97   influence of aerosol mixing state on its hygroscopicity and volatility (Zhang et al., 2016; Cai et al.,

98   2017; Wang et al., 2017). Strong correlations were found between hydrophobic and non-volatile

99   particles, suggesting that they might be of similar chemical composition (Zhang et al., 2016). In

100   addition, some studies showed that except for BC, low-volatility particles correlated well with CCN-

101   inactive particles based on VTDMA and CCNC measurements (Kuwata et al., 2007; Kuwata and

102   Kondo, 2008; Rose et al., 2011; Cheng et al., 2012). Therefore, intercomparisons between mixing

103   state parameters measured by distinct techniques provides not only better characterization of the

104   aerosol mixing state itself, but also insight into aerosol physiochemical properties. Previous studies

105   have mainly compared two kinds of aerosol mixing state measurements, lacking comprehensive

106   comparative analysis among SP2, DMA-CCN, and HV-TDMA measurements, hindering the wide

107   applications of derived aerosol mixing states obtained by individual techniques.

108   The mixing state of primary aerosols can vary greatly depending on their type and emission

109   conditions (Cheng et al. 2012; Wang et al. 2017; Wang et al., 2022; Ting et al., 2018; Liu et al., 2021),

110   and can be significantly altered during aging processes or secondary formations (Wehner et al. 2009;

111   Cheng et al. 2012; Wang et al., 2022; Tomlin et al., 2021; Lata et al., 2021). Primary aerosol emissions

112   such as biomass burning, fossil fuel combustion and cooking tend to contribute to weakly hygroscopic

113   (Herich et al., 2008, 2009; Wang et al., 2020; Kim et al., 2020) and low-volatility aerosols (Hong et

114   al., 2017; Saha et al., 2018), while formation of secondary aerosol including aging of BC-containing

115   aerosols and primary organic aerosols mainly contribute to aerosols with strong CCN activity (Mei et

116   al., 2013; Ma et al., 2016; Tao et al., 2021) and high hygroscopicity (Chen et al., 2018; Kim et al.,

117   2020; Wang et al., 2020). To enhance our understanding of the mixing state of aerosols from different

118   emission sources and to improve its characterization in models, it is important to study the impact of

119   specific primary aerosol emissions and secondary aerosol formations on aerosol mixing states and the

120   influence on aerosol mixing state parameters derived from different techniques.

121   The North China Plain (NCP) is among the most polluted regions in China with various primary

122   emission sources and strong secondary aerosol formations playing critical roles in air pollution (Xu et

123   al., 2011; Tao et al., 2012; Liu et al., 2015). The complex mixing state of aerosols in the NCP

124   contributes to uncertainties in evaluating their climate and environmental effects (Zhuang et al., 2013;

125   Nordmann et al., 2014; Zhang et al., 2016; Tao et al., 2020; Shi et al., 2022), particularly with regards

126   to BC particles (Wu et al., 2017; Liu et al., 2019; Zhao et al., 2019; Wang et al., 2011; Zheng et al.,

127   2019). Meteorological conditions can greatly impact the secondary aerosol formation in the NCP,

128   which can be significantly exacerbated during severe pollution events (Kuang et al., 2020), and

129   consequently affect the aerosol mixing states (Tao et al., 2021). This study obtained aerosol mixing

130   state through concurrent measurements of CCN activity, hygroscopicity, volatility and BC particle at

131   a regional site in the NCP, using CCNC, HTDMA, VTDMA and SP2 instruments. This provides a

132   unique opportunity to perform a most comprehensive intercomparison of aerosol mixing state among

133   different techniques for insights into the impact of primary aerosol emissions and secondary aerosol

134   formations on the observed aerosol mixing states.

135

136   **2 Materials and methods**

137   **2.1 Campaign information and instruments set-up**

138   From 16th October to 16th November 2021, aerosol mixing states were continuously and

139   concurrently monitored using different techniques at the Gucheng site in Dingxing county, Hebei

140   province, China, as part of the campaign of investigating AQueous Secondary aerOsol formations in

141   Fogs and Aerosols and their Radiative effects in the NCP (AQ-SOFAR). The observation site, located

142   at 39°09'N, 115°44'E, is an Ecological and Agricultural Meteorology Station of the Chinese Academy

143   of Meteorological Sciences, situated between the megacities of Beijing (approximately 100 km away)

144   and Baoding (approximately 40 km away), and surrounded by farmlands and small towns. This site

145   provides a representative view of the background conditions of atmospheric pollution in the NCP

146   (Kuang et al., 2020; Li et al., 2021).

147   Different measurement techniques were used during the campaign to simultaneously obtain the

148   aerosol mixing state through CCN activity, hygroscopicity, volatility, and BC particle observations (to

149   be discussed in the next section). In addition to aerosol mixing state measurements, the AQ-SOFAR

150   campaign also included measurements of aerosol number size distribution, chemical composition,

151   aerosol scattering and absorption properties. The total rBC mass concentrations were determined using

152   an aethalometer (Magee, AE33; Drinovec et al., 2015), with more information about the correction of

153   the absorption measurements and mass concentration calculations available in Luo et al. (2022). All

154   aerosol measurement instruments were housed in a temperature-controlled container set at 24 °C.

155   Meteorological data, such as temperature, pressure, wind speed and direction, relative humidity (RH),

156   were obtained from an automatic weather station operated by the station.

157   The chemical composition of submicron aerosols was analyzed using a High-Resolution Time-

158   of-Flight Aerosol Mass Spectrometer (HR-ToF-AMS). The ionization efficiency (IE) was calibrated

159   using 300 nm diameter pure NH_4NO_3 particles, following the standard protocols outlined in Jayne et

160   al. (2000) in the middle of the campaign, with the relative ionization efficiency (RIE) of ammonium

161   determined to be 5.26. The RIE of sulfate was 1.28 using pure $(NH_4)_2SO_4$ particles, and the default

162   RIEs of 1.4 for organic aerosols, 1.1 for nitrates, and 1.3 for chlorides were used. The composition

163   dependent collection efficiency reported by Middlebrook et al. (2012) was used in this study.

164   Elemental ratios were derived using the "Improved-Ambient (I-A)" method as described in

165   Canagaratna et al. (2015), including hydrogen to carbon (H/C), oxygen to carbon (O/C), and organic

166   mass to organic carbon (OM/OC) ratios. Two POA factors and two SOA factors were identified by

167   HR-PMF (Ulbrich et al., 2009; Paatero and Tapper, 1994). The mass spectra of the OA factors and

168   their correlations with external species are shown in Figs. S1-S2. The BBOA spectrum was

169   characterized by obvious m/z 60 (mainly $C_2H_4O_2^+$) and 73 (mainly $C_3H_5O_2^+$), two indicators of

170   biomass burning (Mohr et al., 2009). In addition, BBOA was correlated well with $C_2H_4O_2^+$ (R^2=0.91)

171   and $C_3H_5O_2^+$ (R^2=0.90). Consistent with previous studies in Beijing (Xu et al., 2019), the PMF analysis

172   revealed a mixed factor named FFOA that comprises traffic emissions and coal combustions, which

173   was characterized by typical hydrocarbon ion series. It was observed that FFOA had a relatively high

174   f_{44} (0.083) value, which is likely due to aging during regional transportation, similar to the results

175   observed in the winter of 2016 in Beijing (Xu et al., 2019) and CCOA in Gucheng (Chen et al., 2022).

176   Two SOA factors were found to display different spectral patterns, correlations with tracers and diurnal

Atmospheric
Chemistry
and Physics
Discussions
Open Access
EGU

177   variations, suggesting that they resulted from different chemical processing. For example, OOA1 had

178   higher $CO_2^+/C_2H_3O^+$ (3.9) and O/C (0.91) ratios compared to OOA2 (2.1, 0.78).

179   **2.2 Aerosol mixing states measurement techniques**

180   **2.2.1 DMA-CCNC measurements**

181   The CCN activity of particles under supersaturated conditions was measured using a DMA-

182   CCNC system, which consisted of a differential mobility analyzer (DMA, model 3081 by TSI, Inc.,

183   MN USA), a condensation particle counter (CPC, model 3756 by TSI, Inc., MN USA), and a

184   continuous-flow CCNC (model CCN100 by Droplet Measurement Technologies, USA). The system

185   operated in a size-scanning mode and provided the Size-resolved Particle Activation Ratio (SPAR) by

186   combining the CPC and CCNC measurements at different particle sizes. Three supersaturations (SSs)

187   of 0.08%, 0.14% and 0.22% were applied in a single cycle of about 15 minutes. The sample and sheath

188   flow rates of the DMA were set at 1 lpm and 5 lpm, respectively, resulting in a measured particle

189   diameter range of 9 nm to 500 nm with a running time of 5 minutes per cycle. Supersaturations in the

190   CCNC were calibrated with monodisperse ammonium sulfate particles (Rose et al., 2008) both before

191   and after the campaign. The flow rates were also calibrated before and after the campaign and were

192   checked daily to minimize uncertainties in the droplet counting and supersaturation formed in the

193   column (Roberts and Nenes, 2005; Lance et al., 2006). The SPAR deviations due to multiple-charge

194   particles were corrected using a modified algorithm based on Hagen and Alofs (1983) and Deng et al.

195   (2011). More details about the system can be found in Ma et al. (2016) and Tao et al. (2021).

196   **2.2.2 H/V-TDMA measurements**

197   The mixing state of aerosols in terms of hygroscopicity and volatility was measured using a

198   Hygroscopicity/Volatility Tandem Differential Mobility Analyzer (H/V-TDMA; Tan et al., 2013). The

199   H/V-TDMA consists of two DMA (Model 3081L, TSI Inc.), with the first DMA (DMA1) selecting

200   dried particles and the second DMA (DMA2) selecting conditioned particles. The H/V-TDMA can

201   operate in either H-mode or V-mode, which is controlled by a three-way solenoid valve. In H-mode, a

202   Nafion humidifier is used to condition the selected dry particles to 90% relative humidity (RH)

203   equilibrium. The number size distribution of the humidified particles (Dp) is measured by DMA2 and

204   a CPC (Model 3772, TSI Inc.). The RH-dependent hygroscopic growth factor (GF) at a certain dry

205   diameter is calculated as follows:

206 $$GF=\frac{D_p}{D_d} \qquad\qquad (1)$$

207 In this mode, four dry electrical mobility diameters (50, 100, 150 and 200 nm) were measured. The

208 instrument was regularly calibrated using Standard Polystyrene Latex Spheres (PSL) and Ammonium

209 Sulfate particles.

210 In the V-mode, a heated tube was used to evaporate the volatile coatings from the previously

211 selected dry particles. Six temperature settings were used for the heated tube, ranging from 25 to 200°C.

212 The number size distributions of the heated particles were measured using DMA2 and CPC. Besides

213 the four particle sizes measured in H-mode, three additional particle sizes (250, 300 and 350 nm) were

214 measured in the V mode. The temperature dependent shrinkage factor (SF), which is the ratio of the

215 heated particle size to the dry particle size, is defined as:

216 $$SF=\frac{D_p}{D_d} \qquad\qquad (2)$$

217 A complete cycle of both H-mode measurements at one relative humidity (RH) condition and

218 V-mode measurements at six temperature conditions took approximately 3 hours. A Probability

219 Density Function (PDF) of GF (or SF) can be calculated from the measured density function using the

220 inversion algorithm described by Stolzenburg and McMurry (2008).

2.2.3 DMA-SP2 measurements

222 The size-resolved BC mixing states were measured by the SP2 (Droplet Measurement

223 Technology, Inc., USA) after a DMA (Model 3081, TSI, USA). The DMA selected aerosols at various

224 dry particle sizes, which were then introduced to the SP2. The DMA-SP2 setup was able to measure

225 the mixing states of aerosols at diameters of 100 nm, 120 nm, 160 nm, 200 nm, 235 nm, 270 nm, 300

226 nm, 335 nm, 370 nm, 400 nm, 435 nm, 470 nm, 500 nm, 535 nm, 570 nm, 600 nm, 635 nm, 670 nm,

227 700 nm within 20 minutes, when it wasn't placed after a thermodenuder-bypass switch system.

228 However, it only measured mixing states at diameters of 120 nm, 160 nm, 200 nm, 250 nm, 300 nm,

229 400 nm, and 500 nm when it was placed after a thermodenuder-bypass switch system.

230 The SP2 chamber has a continuous Nd: YAG laser beam at a wavelength of 1064 nm. The BC-

231 containing particles passing through the laser beam will be incandescent through absorbing the

232 radiation. By measuring the intensity of the emitted incandescent light, the mass concentration of BC

233　can be calculated. The sheath flow/sample flow ratio was maintained at 10 for DMA to reduce the

234　width of diameter distribution of selected monodisperse aerosols. Additionally, the flow rate of the

235　SP2 was changed from 0.1 to 0.12 L/min starting on October 22nd. The SP2 was calibrated using

236　Aquadag soot particles, as reported by Gysel et al. (2011). Further details about the calibrations are

237　introduced in Section 1 of the supplement.

238

239　**2.3 Derivations of mixing state parameters**

240　**2.3.1 Fitting SPAR curves measured by the DMA-CCNC system**

241　　　The measured SPAR curves can be parameterized with a sigmoidal function with three parameters.

242　This parameterization assumes that the aerosol is an external mixture of hydrophilic particles that are

243　CCN-active and hydrophobic particles that are CCN-inactive (Rose et al., 2010). The formula used to

244　parameterize SPAR ($R_a(D_d)$) for a specific SS is as follows (Rose et al., 2008):

$$R_a(D_d) = \frac{MAF}{2}\left(1 + \mathrm{erf}\left(\frac{D_d - D_a}{\sqrt{2\pi}\sigma}\right)\right) \tag{7}$$

246　where erf is the error function. MAF is an asymptote of the measured SPAR curve at large particle

247　sizes, and it represents the number fraction of CCNs to total particles. D_a is the midpoint activation

248　diameter and is linked to the hygroscopicity of CCNs. σ is the standard deviation of the cumulative

249　Gaussian distribution function and characterizes the heterogeneity of CCN hygroscopicity. Generally,

250　hydrophilic particles larger than D_a can become CCN, so these three parameters can be used to

251　characterize the hygroscopicity of those hydrophilic particles. This study did not consider the impact

252　of nearly hydrophobic particles on SPAR, as deviations from this parameterization scheme due to this

253　impact are negligible at low SSs, as stated in Tao et al. (2020).

254

255　**2.3.2 Classification of particle type based on hygroscopicity or volatility**

256　　　In this study, ambient aerosol particles were classified into two groups based on their

257　hygroscopicity (hydrophobic and hydrophilic) and two groups based on their volatility (non-volatile

258　and volatile) based on the measurements from H/V-TDMA (Wehner et al., 2009; Liu et al., 2011;

259　Zhang et al., 2016). Each group can be defined using a critical value of GF or SF as the following:

260   Hydrophobic population: $GF < GF_C$;

261   Hydrophilic population: $GF \geq GF_C$;

262   Non-volatile population: $SF \geq SF_C$;

263   Volatile population: $SF < SF_C$.

264   The critical values of GF (GF_C) and SF (SF_C) in H/V-TDMA depend on particle size and working

265   conditions such as relative humidity and heating temperature.

266   During this campaign, the SF_C was set at 0.85 for all seven measured particle sizes at a temperature of

267   200 °C. The GF_C for the four measured particle sizes were 1.1, 1.15, 1.175 and 1.2, respectively, and

268   the corresponding hygroscopicity parameter, κ, was approximately 0.07. These values of GF_C and SF_C

269   divide the probability density functions (PDFs) of SF and GF into two modes, consistent with prior

270   studies in the NCP (Liu et al., 2011; Zhang et al., 2016). The number fraction (NF) for the hydrophilic

271   group (NF_H) and volatile group (NF_V) can be calculated as:

272    $$NF_H = \int_{GF_C}^{\infty} GFPDF(GF)\,dGF \qquad (7)$$

273    $$NF_V = \int_{0}^{SF_C} SFPDF(SF)\,dSF \qquad (8)$$

274   where GFPDF and SFPDF are the PDFs of GF and SF, respectively, derived from H/V-TDMA

275   measurements.

276   **2.3.3 Classification of particle type based on DMA-SP2 measurements**

277   The BC-containing aerosols can be categorized into two groups based on the coating thickness:

278   bare BC/thinly coated BC particles and thickly coated BC particles. The coating thickness of the BC-

279   containing aerosols in the SP2 measurement can be determined by the lag time between the peak of

280   the scattering signal and the incandescence signal (Moteki and Kondo, 2007; Schwarz et al., 2006;

281   Sedlacek et al., 2012; Subramanian et al., 2010; Metcalf et al., 2012). A critical lag-time threshold can

282   be used to differentiate between the different types of BC-containing aerosols and calculate the number

283   fraction of bare BC particles and coated BC particles in the total identified aerosols. In this study, a

284   two-mode distribution of the lag-time (Δt) was observed, and a critical value of 0.8 μs was used to

285   classify the BC-containing particles into thinly coated (or bare) BC ($\Delta t < 0.8$ μs) and thickly coated

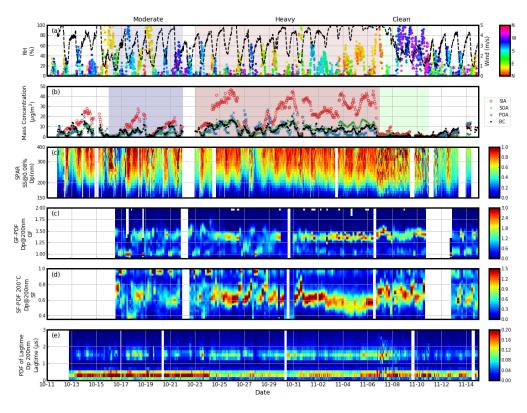286   BC ($\Delta t \geqslant 0.8$ μs), respectively.

287

288   **3 Results and discussions**

289   **3.1 Campaign Overview**

290   The time series of meteorological parameters, SPAR at SS of 0.08%, GF-PDF at

291

Fig 1. Overview of the measurements during the campaign: (a) dots represent wind speed with color indicating wind direction, and black lines represent RH; (b) red circle, green plus, blue x and black dots represent mass concentration of SIA, SOA, POA and BC, respectively; (c) SPAR under SS of 0.08%; (d) PDF of GF (GFPDF) at 200 nm; (e) PDF of SF (SFPDF) at 200 nm and 200 °C; (f) PDF of lag-time at 200 nm. The blue, red and green shaded periods represent the three periods with moderate pollution, heavy pollution and clean condition, respectively.

292   200 nm, SF-PDF at 200 nm and 200 °C, lag-time PDF of 200 nm BC-containing particles and mass

293   concentrations of SIA (secondary inorganic aerosol), SOA (OOA1 and OOA2), PA (BBOA and FFOA)

294   and BC are shown in Fig. 1. During the campaign, three periods with significantly different aerosol

295   pollution conditions were identified. As shown in Fig. 1(b), before October 23rd (moderately polluted

296   period), the accumulation of aerosols led to SIA mass concentrations greater than 20 $\mu g/m^3$, while the

297   highest concentrations of SOA, POA and BC mass all reached 10 $\mu g/m^3$. The mass concentrations of

298   different chemical compositions increased significantly from October 23rd to November 6th (heavily

299   polluted period) and decreased to much lower levels after November 6th(clean period). Two particle

300   groups were identified with regard to CCN activity, hygroscopicity, volatility and coating thickness,

301   as demonstrated by SPAR, GF-PDF, SF-PDF, and the lag-time PDF of BC-containing particles.

302   Significant variations in aerosol mixing states were also observed during the three periods of different

303   pollution conditions, as demonstrated by the variations in SF-PDF measured by the VTDMA. For

304   example, the SF of the non-volatile particle group decreased during the heavily polluted period.

305   Aerosol mixing states may have changed due to various transformations of existing aerosol particles

306   and distinct secondary formation processes under different pollution conditions (Kuang et al., 2020;

307   Tao et al., 2021; Shi et al., 2022; Yang et al., 2022). This will be analyzed in detail later in the

308   discussion. The diurnal variations in mass concentrations of different aerosol chemical compositions

309   and mixing states can be seen in the variations of SPAR measurements, as previously observed in this

310   region (Liu et al., 2011; Ma et al., 2012; Kuang et al., 2015; Tao et al., 2020).

311   In Fig. 2, the campaign averaged SPAR at the three SSs, PDF of lag-time of BC containing

312   particles, GFPDF and SFPDF at 200 °C at different particle sizes are presented. The sigmoidal SPAR

313   curves were characterized by a rapid increase followed by a gradual increase to unit 1, similar to

314   measured SPAR curves previously observed in this region (Deng et al., 2011; Zhang et al., 2014; Ma

315   et al., 2016; Tao et al., 2018). At lower SSs, the rapid increases in SPAR curves occur at larger particle

316   sizes and the maximum AR of SPAR curves becomes smaller. For the three measured SSs, the

317   corresponding fitting parameters, Da, which indicate the center of the particle size range with rapid

318   increases in SPAR curves, are approximately 90 nm, 120 nm and 180 nm, respectively. The number

319   fraction of CCN-active particles in large diameter ranges (which varies with SS and, for example, is

320   greater than 200 nm for 0.08%) can be indicated by the gradual increase of SPAR curves and quantified

321   by the fitting parameter, MAF. The PDFs of the lag-time, GF, and SF are all characterized by a bimodal
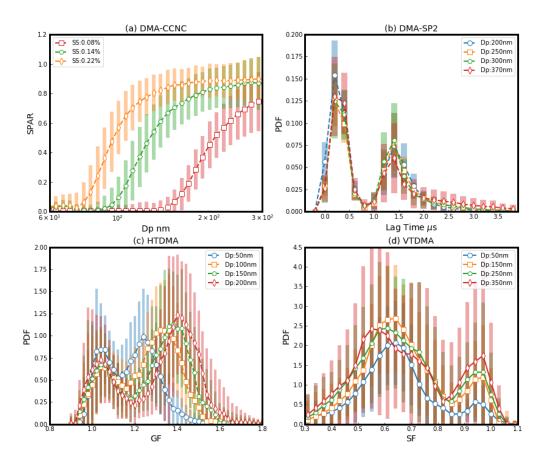
Fig. 2. The campaign average of (a) SPAR curves measured by DMA-CCNC at the three SSs (identified by colors and markers), (b) PDF of lag-time measured by DMA-SP2 at four particle sizes (identified by colors and markers), (c) PDF of GF (GFPDF) measured by HTDMA at four particle sizes (identified by colors and markers), (d) PDF of SF (SFPDF) measured by VTDMA under the temperature of 200 °C at five particle sizes (identified by colors and markers).

323　distribution, which indicates two particle groups of BC-containing aerosols with different coating

324　thickness, hygroscopicity and volatility. The variations in aerosol mixing state will be further

325　analyzed on the basis of MAF and the number fractions (NF) of hydrophilic particles (NF_H), volatile

326　particles (NF_V), BC-free particles (NF_{noBC}) and number fractions of thinly coated BC in BC containing

327　aerosols (R_{exBC}).

328

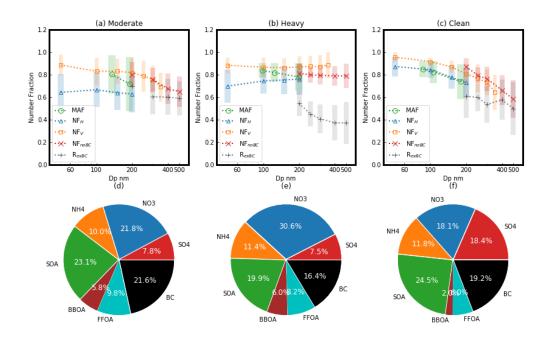329　**3.2 Intercomparisons among aerosol mixing state parameters derived using four techniques**

Fig. 3. (a-c): Size dependence of MAF (green circle), NF_H (blue triangle), NF_V at 200 °C (yellow square), NF_{noBC} (red x) and R_{exBC} (black plus) during the three periods. (d-f): Corresponding mass fractions of aerosol chemical compositions (identified by colors) during the three periods.

330   The size dependence of MAF, NF_H, NF_V (200 °C), NF_{noBC} and R_{exBC} during the three pollution

331   periods are shown in Fig 3. In general, the size dependence of MAF, NF_H, NF_V and NF_{noBC} were

332   similar to one another, suggesting they were dominated by the same particle group, namely BC-free

333   particles. This particle group had the lowest fraction during the heavily polluted period and the highest

334   fraction during the clean period, with the fraction decreasing with particle size This suggests that

335   primary emissions tend to have higher fractions of BC-containing particles in larger diameter ranges.

336   Since the bulk aerosol mass fraction (MF) is mostly contributed by particles larger than 300 nm, there

337   might have been more hydrophilic, volatile, CCN-active and BC-free particles in larger sizes (> 300

338   nm) during the heavily polluted period, due to strong secondary aerosol formation in larger diameter

339   ranges (Kuang et al., 2020), resulting in higher number fraction of these particles compared to the

340   clean period. As for R_{exBC}, the small size dependence of R_{exBC} during the moderately polluted period

341   might have been associated with stronger primary emissions, while the decrease of R_{exBC} with

342   increasing particle diameter size in the polluted period confirms the more efficient secondary aerosol

343   formation in larger diameter ranges.

344   As for the difference among the aerosol mixing state parameters, NF_V and NF_{noBC} agreed with

345   each other with a difference smaller than 0.1, and both were higher by at least 0.1 than NF_H in the

346   moderately polluted period. In detail, compared to NF_{noBC}, NF_V was higher during the heavily polluted

347   period, when the nitrate fraction was the highest and the SOA fraction was the lowest among all three

348   periods, suggesting some BC-containing aerosols in this period were also identified as volatile, which

349   is consistent with the fact that formation of semi-volatile nitrate in the BC-containing particles

350   increases their volatility. However, during the clean period, NF_V was even lower than NF_{noBC},

351   suggesting that some BC-free aerosols were characterized as low volatile and non-negligible fractions

352   of BC-free aerosols dominated within these less volatile aerosol components, which were likely less

353   volatile organic aerosols. In addition, the MAF values generally agreed with NF_H during the clean

354   period, but were larger than NF_H during the moderately and heavily polluted periods when the

355   POA/SOA fractions were higher. POA generally had lower hygroscopicity than SOA. The critical κ

356   of hydrophilic mode aerosols was 0.07, suggesting that a higher fraction of aerosols had κ below 0.07

357   during the moderately polluted period. However, under supersaturated conditions, they demonstrated

358   enhanced hygroscopicity by becoming CCN-active. The NF_H was consistently lower than NF_V and

359   NF_{noBC} (the average difference between NF_H and NF_{noBC} was about 0.2), especially during the

360   moderately polluted period, suggesting a significant fraction of volatile BC-free aerosols had

361   hygroscopicity lower than 0.07 but were still CCN-active and therefore not fully hydrophobic.

362   The diurnal variations of MAF, NF_H, NF_V and NF_{noBC} along with the mass fractions of aerosol

363   chemical compositions during the three periods, are shown in Fig.4. With the exception of particle size

364   50 nm, the diurnal variations of these four mixing state parameters were generally similar for all

365   measured sizes. The different diurnal variations at particle size 50 nm may be due to the different

366   effects   of   emissions
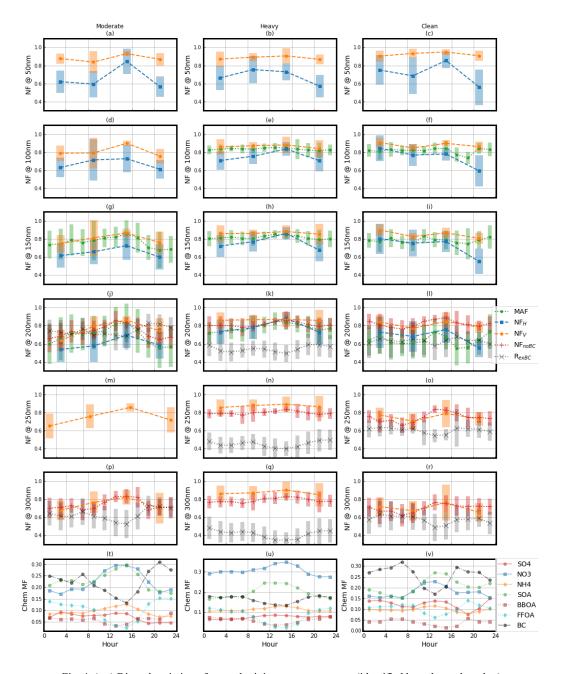
367

Fig. 4. (a-r) Diurnal variation of aerosol mixing state parameters (identified by color and marker) at different particle size during the three periods. (t-v) Diurnal variation of mass fraction of aerosol chemical compositions (identified by color and marker) during the three periods.

368   and aging processes on different aerosol modes, as particles smaller than 100nm were mainly in a

369 different aerosol mode (Aitken mode) to particles larger than 100nm (Wang et al., 2022). For particle

370 sizes larger than 100 nm, there were peaks in the afternoon for MAF, NF_H, NF_V and NF_{noBC}, due to

371 the increase in secondary aerosol compositions like nitrate and SOA, and the decrease of POA and BC.

372 The diurnal variations of aerosol mixing state parameters and aerosol chemical compositions were

373 more pronounced in the moderately polluted period. During the heavily polluted period, the diurnal

374 variation was least pronounced for NF_V and most pronounced for NF_H. In the clean period, there was

375 another peak at midnight for MAF and NF_{noBC}, which may be attributed to the diurnal variations of

376 secondary aerosol compositions like sulfate and SOA, and the decrease of BC and FFOA. The average

377 size-dependence of the aerosol mixing state parameters in different time ranges during the heavily

378 polluted period is shown in Fig. S3. It can be seen that the differences among the four parameters were

379 the least from 12:00 to 18:00, with the most SOA and the least POA. This is consistent with the results

380 in Fig.3, where the difference between MAF and NF_H becomes smaller when POA fractions are the

381 smallest. In general, the diurnal variations for R_{exBC} are opposite to those of NF_{noBC} and agree better

382 with those of the primary aerosol mass fractions.

383 The intercomparisons among MAF, NF_H, NF_V and NF_{noBC} were conducted based on their

384 correlations at different particle sizes as summarized in Table. S1. It's worth noting that MAF at SSs

385 of 0.08%, 0.14% and 0.22% was used for comparison at particle sizes of 200 nm, 150 nm and 100 nm,

386 respectively. In general, there were moderate correlations among MAF, NF_H and NF_V, suggesting the

387 dominance of CCN-active, hygroscopic and volatile aerosols are contributed by a similar particle

388 group (Zhang et al., 2016). The consistency of MAF-NF_V was slightly higher than that of MAF-NF_H

389 or NF_H-NF_V with similar correlation coefficients (~0.65) but smaller systematic differences (slope and

390 intercept were much closer to 1 and 0, respectively), which is consistent with the previous finding that

391 a substantial fraction of volatile but less hygroscopic aerosols is CCN-active. At smaller particle size,

392 the correlation became weaker, while the degree was the least for the correlation between MAF and

393 NF_V.

394

3.3 Impacts of primary aerosol emissions on aerosol mixing states and parameter intercomparisons
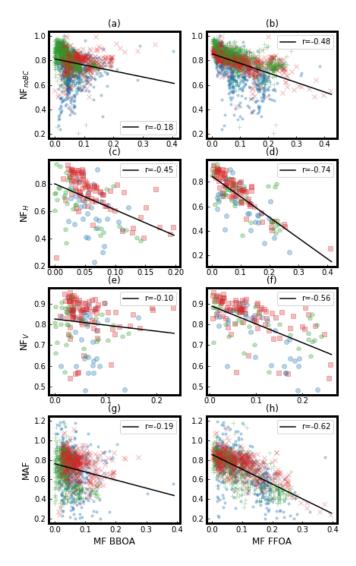

Fig. 5. The correlation between aerosol mixing state parameters and MF of primary organic aerosol chemical composition during different periods. Moderately polluted period: Blue dot or circle; Heavily polluted period: Red x or square; Clean period: Green plus or pentagon.

In Fig. 5, the correlation between each aerosol mixing state at 200 nm and the mass fraction of each primary organic aerosol composition during the three periods is presented. In general, these four mixing state parameters were negatively correlated with MF_{FFOA} and MF_{BBOA}. However, the
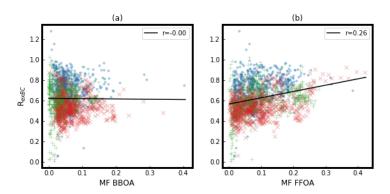
19

Atmospheric
Chemistry
and Physics
Discussions

Fig. 6. The correlation between the ratio of external mixed BC in total BC particles and MF of primary organic aerosol chemical composition during different periods. Moderately polluted period: Blue dot; Heavily polluted period: Red x; Clean period: Green plus.

400 correlation with MF_{FFOA} was much weaker compared to MF_{BBOA}. Biomass burning emissions and

401 fossil fuel emissions are two major sources of BC in the NCP (Yang et al., 2022), and NF_{noBC} was

402 negatively correlated with MF_{FFOA} (r=-0.49) and weakly correlated (r=-0.18) with MF_{BBOA}, suggesting

403 that fossil fuel emission were the more likely source of BC during this field campaign. The negative

404 correlation between MAF and MF_{FFOA} was even weaker than that of NF_{noBC} with MF_{FFOA} (-0.62 vs. -

405 0.49). Especially, at the same MF_{FFOA}, MAF was lower than NF_{noBC}, demonstrating that some BC-free

406 particles were CCN-inactive, and likely mainly composed of organic aerosols from fossil fuel

407 combustion emission. The negative correlation between NF_V and MF_{FFOA} was slightly weaker than

408 that between NF_{noBC} and MF_{FFOA} (-0.56 vs -0.49). At the same MF_{FFOA}, NF_{noBC} was close to NF_V, and

409 considering that BC-containing aerosols were dominated by thinly coated BC during most times (as

410 shown in Fig.5), this demonstrates that the non-volatile population identified by the V-TDMA was

411 mainly contributed by BC-containing aerosols. NF_H had the lowest negative correlation with MF_{FFOA}

412 (r=-0.74), demonstrating the significant contributions from fossil fuel emissions to nearly hydrophobic

413 aerosol populations. At the same MF_{FFOA}, the NF_H was obviously lower than NF_{noBC} (larger and

414 smaller than 0.7 when MF_{FFOA} was larger than 0.1, respectively), demonstrating that a substantial

415 portion of nearly hydrophobic aerosols was not contributed by BC-containing aerosols, but likely by

416 FFOA or BBOA dominant aerosols (NF_H also had a negative correlation with MF_{BBOA}). However, the

417 markedly different correlations between MAF with MF_{FFOA} (r=-0.62) and between MAF with MF_{BBOA}

418 (r=-0.2) imply that those nearly hydrophobic but CCN-active aerosols were likely contributed by

Atmospheric
Chemistry
and Physics
Discussions

Open Access

EGU

419 biomass burning emissions. The correlations between the ratio of thinly coated BC in total BC-

420 containing particles and the mass fractions of BBOA and FFOA are shown in Fig.6, and weak

421 correlations between R_{exBC} with MF_{BBOA} and MF_{FFOA} are observed. However, R_{exBC} tended to increase

422 with MF_{FFOA}, suggesting that BC containing aerosols emitted from fossil fuel combustion tended to be

423 more externally mixed with other aerosol components than those emitted from biomass burning
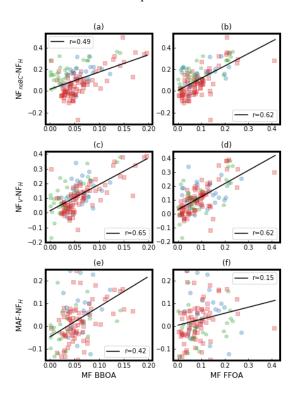

Fig. 7. The correlation between the difference among the four aerosol mixing state parameters and MF of primary organic aerosol chemical composition during different periods. Moderately polluted period: Blue circle; Heavily polluted period: Red square; Clean period: Green pentagon.

424 activities. These results demonstrate remarkably different mixing states as well as physical and

425 chemical properties of fossil fuel combustion aerosols and biomass burning aerosols.

426   The impact of primary emissions on the differences among the four aerosol mixing state

427 parameters is analyzed and shown in Fig. 7. The difference between $NF_{noBC}-NF_H$ and NF_V-NF_H both

428 had strong positive correlations with MF_{FFOA} and MF_{BBOA} (r>0.5), suggesting that a substantial

429 proportion of POA resided in BC-free aerosols and was volatile but contributed substantially to nearly

430   hydrophobic aerosols. The mass fractions of BBOA and FFOA were poorly linked with the difference

431   between MAF-NF_V or MAF-NF_{noBC} or NF_V-NF_{noBC} (Fig. S5). The difference between MAF-NF_H had

432   a positive correlation with MF_{BBOA}, further suggesting BBOA contributed to nearly hydrophobic

433   aerosols under subsaturated conditions, however, their hygroscopicity was enhanced and became

434   CCN-active at supersaturated conditions.

435

3.4 Impacts of secondary aerosol formations on aerosol mixing states and parameter

436

437   **intercomparisons**

438   The correlations between each aerosol mixing state parameter at 200 nm and the mass fraction of

439   each secondary aerosol component are presented in Fig. 8 for three periods and the entire campaign

440   are presented. Generally, MAF, NF_H, NF_V and NF_{noBC} had a strong positive correlation with

441   ammonium. This is likely due to the fact that ammonium was mainly formed through the neutralization

442   of sulfuric and nitric acid with ammonia, so variations in ammonium better represent overall secondary

443   inorganic aerosol formation. As shown in Fig.3, the secondary inorganic aerosol components

444   dominated over SA (about 50% vs about 70%), indicating that secondary aerosol formations were

445   primarily composed of secondary inorganic aerosol formation, which explains the weaker correlations

446   with SOA seen in Fig. 8.

447   During the clean period when the mass fraction of SOA and sulfate were both above 15%, all four

448   parameters had a strong positive correlation with MF_{SO4} and MF_{SOA} (r>0.5), suggesting that when

449   clean background airmass with higher fractions of sulfate and SOA prevailed, local primary emissions

450   that contributed substantially to BC-containing and less hygroscopic POA aerosols became less

451   significant. The positive correlations between MAF and secondary aerosol components have been

452   extensively discussed by Tao et al. (2021), who found that secondary aerosol formations enhance the

453   hygroscopicity of nearly hydrophobic aerosols, thereby increasing CCN activity. This also explains

454   the highest correlations of NF_H or MAF with ammonium formation. The strong positive correlations

455   between NF_V and secondary aerosol formations are consistent with the fact that nitrate dominates

456   secondary aerosol formations during this campaign and nitrate is semi-volatile. For the first time, the

457   strong positive correlations between NF_{noBC} and secondary aerosol formations were revealed. This is

458   because NF_{noBC} primarily depends on the relative variations of BC-containing and BC-free aerosols.
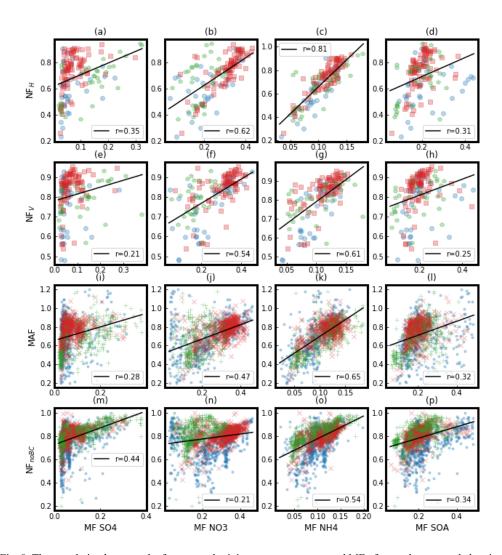
Fig. 8. The correlation between the four aerosol mixing state parameters and MF of secondary aerosol chemical composition during different periods. Moderately polluted period: Blue dot or circle; Heavily polluted period: Red x or square; Clean period: Green plus or pentagon.

459   The increase in NF_{noBC} at 200 nm as a function of secondary aerosol mass fraction suggests that

460   secondary aerosol formations migrated a higher fraction of BC-free aerosols smaller than 200 nm to

461   200 nm, highlighting that secondary aerosols tended to form more quickly on BC-free aerosols than

462   on BC-containing aerosols.

463   The effects of secondary aerosol formation on the differences between the four aerosol mixing

464   state parameters were studied and illustrated in Fig. 9. Differences between NF_{noBC}-NF_H and NF_V-NF_H

465 both showed a strong negative correlation with MF_{NH4} and MF_{NO3}. As previously noted, NF_H typically
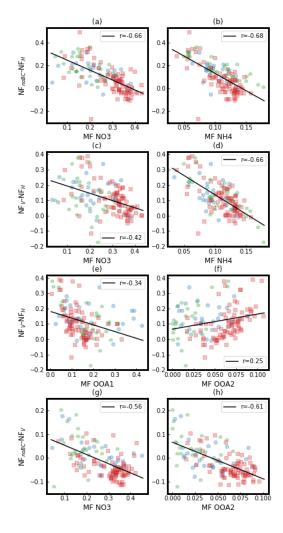

Fig. 9. The correlation between the difference among the four aerosol mixing state parameters and MF of secondary aerosol chemical composition during different periods. Moderately polluted period: Blue circle; Heavily polluted period: Red square; Clean period: Green pentagon.

466 had smaller values than NF_V and NF_{noBC}. Thus, a negative correlation with the mass fraction of

467 ammonium and nitrate indicates that the formation of secondary nitrate results in a smaller difference

468 between these mixing state parameters. The increase in the fraction of ammonium nitrate, a pure

469 scattering semi-volatile compound with strong hygroscopicity, can render the aerosol population more

470 dominated by particles with strong volatility and hygroscopicity. This can result in a smaller difference

471 between NF_{noBC}, NF_H, and NF_V as the secondary inorganic aerosol components increases. Furthermore,

472 the difference between NF_V-NF_H showed a positive correlation with MF_{OOA2} and a negative correlation

473 with MF_{OOA1}, indicating different volatility and hygroscopicity of the two SOA factors. The variations

474 in the difference between NF_V and NF_H with the mass fraction of OOA1 and OOA2 are shown in Fig.

475 9(e) and (f). As previously noted, NF_V was generally higher than NF_H, and the difference between the

476 two decreases with an increase in MF_{OOA1}, which were generally smaller than 0.3. This suggests that

477 the formation of OOA1 enhances the hygroscopicity of volatile particles, which aligns with the highest

478 oxidation state of OOA1 (higher O/C but lower H/C compared to OOA2), which had significant and

479 overall positive impact on aerosol hygroscopicity (Cerully et al., 2015; Thalman et al., 2017; Zhang et

480 al., 2023). A positive correlation is seen between NF_V and MF_{OOA2} (r=~0.25), whereas the correlation

481 between NF_H and MF_{OOA2} is weak (R is close to 0), implying that OOA2 might be semi-volatile but

482 only weakly hygroscopic, which could contribute to NF_V being higher than NF_H as OOA1 increases.

483 The difference between NF_{noBC}-NF_V is negatively correlated with MF_{NO3}, which is consistent with the

484 semi-volatile nature of nitrate. The negative correlation between NF_{noBC}-NF_V and MF_{OOA2} indicates

485 that the difference is smaller when there is more OOA2, implying that OOA2 are also semi-volatile

486 compounds and were likely formed mainly on BC-free particles. The correlations between the

487 difference between NF_V-MAF and NF_{noBC}-MAF and the mass fraction of each secondary aerosol

488 composition are much weak. The impacts of secondary aerosol formation on BC mixing states are

489 depicted in Fig. S4. In general, the number fraction of thinly coated BC has a negative correlation with

490 SIA and a weak association with SOA, suggesting that SIA formation mainly enhances the thickness

491 of BC coating.

492   In addition to the changes in the mass fractions of secondary aerosol compositions, the

493 accumulation of pollution due to secondary aerosols may also provide insight into the impact of

494 secondary aerosol formations on aerosol mixing states. As shown in Fig. 10 (a), during the heavily

495 polluted periods, there were two distinct pollution accumulation processes from Oct 23rd to Oct 27th

496 and from Oct 28rd to Oct 31st, respectively. During the pollution accumulation process, the mass

497 concentration of secondary aerosols increased by approximately three times, indicating rapid

498 formation of secondary compositions and causing a significant rise in PM mass concentration. Fig. 10

499 (b and c) illustrates that this increase in secondary aerosols led to a significant enhancement of aerosol
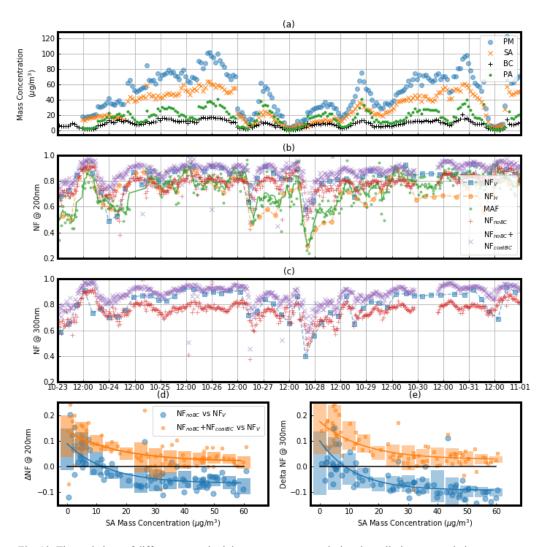
Fig. 10. The variations of different aerosol mixing state parameters during the pollution accumulation process.
(a) The mass concentration of PM, SA, PA and BC (identified by colors and markers). (b and c) The variations
of different aerosol mixing state parameters (identified by colors and markers) at particle size of 200nm (b) and
300nm (c); (d and e) The variations of the difference between NF_V-NF_{noBC} (blue large circle) and NF_V-
$NF_{noBC+CBC}$ (yellow small circle) with the mass concentration of SA at particle size of 200nm (d) and 300nm (e).

500   mixing state parameters, including MAF, NF_V, NF_H and NF_{noBC}, which rose from about 0.5 to about

501   0.8 with evident diurnal variations. This highlights the impact of secondary aerosol formations on

502   aerosol mixing states and the importance of studying the pollution accumulation processes of

503   secondary aerosols. The enhancements of different aerosol mixing state parameters during the

504 pollution accumulation process were not uniform. MAF and NF_H initially showed lower values

505 compared to NF_V and NF_{noBC}, but their later enhancement was stronger than that of NF_{noBC}. Fig. 10 (d)

506 and (e) show the difference between NF_{noBC} and NF_V at 200 nm and 300 nm as a function of secondary

507 aerosol mass concentrations during these two pollution periods, which clearly displays how during

508 secondary aerosol formations NF_V became higher than NF_{noBC} while NF_V kept close to NF_{noBC} plus

509 the number fraction of thickly coated BC containing aerosols. The results suggest that secondary

510 aerosol formation increases the volatility of BC-free and BC-containing aerosols, leading increased

511 NF_V compared to NF_{noBC}. And almost all BC-free particles and some BC-containing aerosols became

512 volatile during the pollution accumulation process.

513

514 **4. Conclusions**

515 The aerosol mixing state is one of the most important physicochemical properties of aerosol

516 particles, which has significant impacts on the optical properties and CCN activity of aerosol particles.

517 Aerosol mixing state varies largely under complex aerosol emissions and atmospheric transformations.

518 In this study, aerosol mixing states derived from CCN activity, hygroscopicity, volatility and BC

519 particles observations, along with their relationship to primary aerosols emissions and secondary

520 aerosol formations, were systematically analyzed based on simultaneous measurements of a CCNC, a

521 H/VTDMA and a SP2. Statistical analysis demonstrated that the number fraction of CCN-active,

522 hygroscopic and volatile particles were generally positively correlated to one another and were

523 contributed mainly by BC-free aerosols. Therefore, NF_{noBC}, MAF, NF_H, and NF_V were all negatively

524 correlated to either MF_{FFOA} or MF_{BBOA}, because fossil fuel combustion and biomass burning were two

525 major sources of BC-containing aerosols during this field campaign. However, differences among

526 these mixing state parameters varied much under different conditions.

527 The intercomparison results highlight the differences in aerosol mixing states and physiochemical

528 properties caused by fossil fuel combustion and biomass burning emissions. CCN and SP2

529 measurements showed that CCN-inactive, BC-free particles were mainly produced by fossil fuel

530 combustion. On the other hand, the comparison between VTDMA and SP2 measurements indicated

531 that non-volatile aerosols were mostly composed of BC-containing particles. The comparison between

532 HTDMA and SP2 measurements revealed that a significant proportion of nearly hydrophobic aerosols

533   was not from BC-containing particles, but from fossil fuel combustion or biomass burning dominated

534   organic aerosols. The correlation between CCNC and HTDMA measurements also showed that nearly

535   hydrophobic, BC-free aerosols can become CCN-active under supersaturated conditions and were

536   tightly linked to biomass burning emissions. This suggests that biomass burning aerosols might exhibit

537   different hygroscopicity under sub- and super- saturated conditions (Bougiatioti et al., 2016).

538   Furthermore, the correlation analysis between SP2 measurements and mass fractions of BBOA and

539   FFOA indicated that BC-containing aerosols from fossil fuel combustion tend to be more externally

540   mixed with other aerosol compositions compared to those from biomass burning activities.

541   Other than primary aerosol emissions, secondary aerosol formations also exerted significant

542   impacts on variations of aerosol mixing states. During this campaign, the secondary aerosol formation

543   was dominated by nitrate and SOA production, which have markedly different impacts on aerosol

544   mixing states due to their different physical properties and formation pathways. NF_{noBC}, MAF, $NF_{H,}$

545   and NF_V were all positively correlated with nitrate and SOA mass fractions, revealing much stronger

546   correlations to SOA than with nitrate. This is consistent with the semi-volatile but highly hygroscopic

547   properties of nitrate. The high correlation coefficient between NF_{noBC} and the mass fractions of

548   secondary aerosols at 200 nm and 300 nm suggests that secondary aerosol formation led to the

549   migration of BC-free aerosols towards larger diameters more quickly than BC-containing aerosols.

550   This outcome reveals that secondary aerosols formed more rapidly on BC-free aerosols than on BC-

551   containing aerosols, which is in line with the BC-containing aerosols' hydrophobic nature that does

552   not favor aqueous secondary aerosol formation. Moreover, as the mass fractions of nitrate or

553   ammonium increased, the differences among mixing state parameters (NF_{noBC}, MAF, NF_H and NF_V)

554   mostly decreased due to the hygroscopic and semi-volatile nature of ammonium nitrate. However, the

555   two resolved SOA factors exhibited different impacts on NF_V-NF_H, and their correlations with NF_V

556   and NF_H revealed that OOA1 was more hygroscopic but less volatile, suggesting distinct formation

557   mechanisms for the two OOA factors during the field campaign.

558   The findings of this study highlight markedly different effects of primary emissions and

559   secondary aerosol formations on aerosol mixing states and suggest that comparisons of aerosol mixing

560   states obtained using various techniques are useful for gaining insights into the hygroscopicity,

561   volatility, and CCN activity of different aerosols. These comparisons can also indicate the impacts of

562   secondary aerosol formations on aerosol physical properties, which can help to understand the

563   pathways of secondary aerosol formation. However, it is important to be cautious in the application of

564   aerosol mixing state parameters, as the suitability of VTDMA-derived mixing state parameters in

565   representing BC mixing states is largely dependent on the composition and mass of secondary aerosols.

566

567   **Data availability**. The data used in this study are available from the corresponding author upon request

568   Ye Kuang (kuangye@jnu.edu.cn) and Li Liu (liul@gd121.cn)

569   **Competing interests**. The authors declare that they have no conflict of interest.

570

571   **Author Contributions**.

572   YK and WY planned this campaign and YK designed the aerosol experiments and conceived this

573   research together with JC, and JC wrote the manuscript. JC performed measurements of CCNC, BL

574   performed measurements of SP2 and analyzed SP2 datasets with the help of GZ, WQ and YL

575   performed AMS measurements, LL performed HV-TDMA measurements and conducted post-data

576   processing as well as some of data analysis. BX, HX, MMZ, HZ and SR participated this campaign

577   and helped instruments maintenance. GZ provided full support for the campaign. All authors

578   contributed to discussions and revisions of this paper.

583

584   **References**

585   Adachi, K., Sedlacek, A. J., Kleinman, L., Chand, D., Hubbe, J. M., and Buseck, P. R.: Volume
586   changes upon heating of aerosol particles from biomass burning using transmission electron
587   microscopy, Aerosol Science and Technology, 52, 46–56,
588   https://doi.org/10.1080/02786826.2017.1373181, 2018.

589   Adachi, K., Sedlacek, A. J., Kleinman, L., Springston, S. R., Wang, J., Chand, D., Hubbe, J. M.,
590   Shilling, J. E., Onasch, T. B., Kinase, T., Sakata, K., Takahashi, Y., and Buseck, P. R.: Spherical tarball
591   particles form through rapid chemical and physical changes of organic matter in biomass-burning
592   smoke, Proceedings of the National Academy of Sciences, 116, 19336–19341,
593   https://doi.org/10.1073/pnas.1900129116, 2019.

594   Bond, T. C., Doherty, S. J., Fahey, D. W., Forster, P. M., Berntsen, T., DeAngelo, B. J., Flanner,
595   M. G., Ghan, S., Kaercher, B., Koch, D., Kinne, S., Kondo, Y., Quinn, P. K., Sarofim, M. C., Schultz,
596   M. G., Schulz, M., Venkataraman, C., Zhang, H., Zhang, S., Bellouin, N., Guttikunda, S. K., Hopke,
597   P. K., Jacobson, M. Z., Kaiser, J. W., Klimont, Z., Lohmann, U., Schwarz, J. P., Shindell, D.,
598   Storelvmo, T., Warren, S. G., and Zender, C. S.: Bounding the role of black carbon in the climate
599   system: A scientific assessment, Journal of Geophysical Research-Atmospheres, 118, 5380–5552,
600   https://doi.org/10.1002/jgrd.50171, 2013.

601   Bougiatioti, A., Bezantakos, S., Stavroulas, I., Kalivitis, N., Kokkalis, P., Biskos, G.,
602   Mihalopoulos, N., Papayannis, A., and Nenes, A.: Biomass-burning impact on CCN number,
603   hygroscopicity and cloud formation during summertime in the eastern Mediterranean, Atmos. Chem.
604   Phys., 16, 7389–7409, https://doi.org/10.5194/acp-16-7389-2016, 2016.

605   Cai, M., Tan, H., Chan, C. K., Mochida, M., Hatakeyama, S., Kondo, Y., Schurman, M. I., Xu,
606   H., Li, F., Shimada, K., Li, L., Deng, Y., Yai, H., Matsuki, A., Qin, Y., and Zhao, J.: Comparison of
607   Aerosol Hygroscopcity, Volatility, and Chemical Composition between a Suburban Site in the Pearl
608   River Delta Region and a Marine Site in Okinawa, Aerosol and Air Quality Research, 17, 3194–3208,
609   https://doi.org/10.4209/aaqr.2017.01.0020, 2017.

610   Canagaratna, M. R., Jimenez, J. L., Kroll, J. H., Chen, Q., Kessler, S. H., Massoli, P., Hildebrandt
611   Ruiz, L., Fortner, E., Williams, L. R., Wilson, K. R., Surratt, J. D., Donahue, N. M., Jayne, J. T., and
612   Worsnop, D. R.: Elemental ratio measurements of organic compounds using aerosol mass
613   spectrometry: characterization, improved calibration, and implications, Atmos. Chem. Phys., 15, 253–
614   272, https://doi.org/10.5194/acp-15-253-2015, 2015.

615   Cerully, K. M., Bougiatioti, A., Hite Jr., J. R., Guo, H., Xu, L., Ng, N. L., Weber, R., and Nenes,
616   A.: On the link between hygroscopicity, volatility, and oxidation state of ambient and water-soluble
617   aerosols in the southeastern United States, Atmos. Chem. Phys., 15, 8679–8694,
618   https://doi.org/10.5194/acp-15-8679-2015, 2015.

619   Chen, C., Qiu, Y., Xu, W., He, Y., Li, Z., Sun, J., Ma, N., Xu, W., Pan, X., Fu, P., Wang, Z., and
620   Sun, Y.: Primary Emissions and Secondary Aerosol Processing During Wintertime in Rural Area of
621   North China Plain, Journal of Geophysical Research: Atmospheres, 127, e2021JD035430,
622   https://doi.org/10.1029/2021JD035430, 2022.

623   Chen, J., Budisulistiorini, S. H., Miyakawa, T., Komazaki, Y., and Kuwata, M.: Secondary
624   aerosol formation promotes water uptake by organic-rich wildfire haze particles in equatorial Asia,
625   Atmos. Chem. Phys., 18, 7781–7798, https://doi.org/10.5194/acp-18-7781-2018, 2018.

626   Cheng, Y. F., Su, H., Rose, D., Gunthe, S. S., Berghof, M., Wehner, B., Achtert, P., Nowak, A.,
627   Takegawa, N., Kondo, Y., Shiraiwa, M., Gong, Y. G., Shao, M., Hu, M., Zhu, T., Zhang, Y. H.,
628   Carmichael, G. R., Wiedensohler, A., Andreae, M. O., and Pöschl, U.: Size-resolved measurement of
629   the mixing state of soot in the megacity Beijing, China: diurnal cycle, aging and parameterization,
630   Atmos. Chem. Phys., 12, 4477–4491, https://doi.org/10.5194/acp-12-4477-2012, 2012.

631   Ching, J., Fast, J., West, M., and Riemer, N.: Metrics to quantify the importance of mixing state
632   for CCN activity, Atmos. Chem. Phys., 17, 7445–7458, https://doi.org/10.5194/acp-17-7445-2017,
633   2017.

634   Ching, J., Adachi, K., Zaizen, Y., Igarashi, Y., and Kajino, M.: Aerosol mixing state revealed by
635   transmission electron microscopy pertaining to cloud formation and human airway deposition, npj
636   Climate and Atmospheric Science, 2, 22, https://doi.org/10.1038/s41612-019-0081-9, 2019.

637   Deng, Z. Z., Zhao, C. S., Ma, N., Liu, P. F., Ran, L., Xu, W. Y., Chen, J., Liang, Z., Liang, S.,
638   Huang, M. Y., Ma, X. C., Zhang, Q., Quan, J. N., Yan, P., Henning, S., Mildenberger, K., Sommerhage,
639   E., Schäfer, M., Stratmann, F., and Wiedensohler, A.: Size-resolved and bulk activation properties of
640   aerosols in the North China Plain, Atmos. Chem. Phys., 11, 3835–3846, https://doi.org/10.5194/acp-
641   11-3835-2011, 2011.

642   Deng, Z. Z., Zhao, C. S., Ma, N., Ran, L., Zhou, G. Q., Lu, D. R., and Zhou, X. J.: An examination
643   of parameterizations for the CCN number concentration based on in situ measurements of aerosol
644   activation properties in the North China Plain, Atmos. Chem. Phys., 13, 6227–6237,
645   https://doi.org/10.5194/acp-13-6227-2013, 2013.

646   Drinovec, L., Močnik, G., Zotter, P., Prévôt, A. S. H., Ruckstuhl, C., Coz, E., Rupakheti, M.,
647   Sciare, J., Müller, T., Wiedensohler, A., and Hansen, A. D. A.: The "dual-spot" Aethalometer: an
648   improved measurement of aerosol black carbon with real-time loading compensation, Atmos. Meas.
649   Tech., 8, 1965–1979, https://doi.org/10.5194/amt-8-1965-2015, 2015.

650   Ervens, B.: Modeling the Processing of Aerosol and Trace Gases in Clouds and Fogs, Chemical
651   Reviews, 115, 4157–4198, https://doi.org/10.1021/cr5005887, 2015.

652   Farmer, D. K., Cappa, C. D., and Kreidenweis, S. M.: Atmospheric Processes and Their
653   Controlling Influence on Cloud Condensation Nuclei Activity, Chemical Reviews, 115, 4199–4217,
654   https://doi.org/10.1021/cr5006292, 2015.

655   Fierce, L., Riemer, N., and Bond, T. C.: Toward Reduced Representation of Mixing State for
656   Simulating Aerosol Effects on Climate, Bulletin of the American Meteorological Society, 98, 971–
657   980, https://doi.org/10.1175/BAMS-D-16-0028.1, 2017.

658   Fu, Y., Peng, X., Sun, W., Hu, X., Wang, D., Yang, Y., Guo, Z., Wang, Y., Zhang, G., Zhu, J.,
659   Ou, J., Shi, Z., Wang, X., and Bi, X.: Impact of Cloud Process in the Mixing State and Microphysical
660   Properties of Soot Particles: Implications in Light Absorption Enhancement, Journal of Geophysical
661   Research: Atmospheres, n/a, e2022JD037169, https://doi.org/10.1029/2022JD037169, 2022.

662   Gysel, M., Laborde, M., Olfert, J. S., Subramanian, R., and Gröhn, A. J.: Effective density of
663   Aquadag and fullerene soot black carbon reference materials used for SP2 calibration, Atmos. Meas.
664   Tech., 4, 2851–2858, https://doi.org/10.5194/amt-4-2851-2011, 2011.

665   Herich, H., Kammermann, L., Gysel, M., Weingartner, E., Baltensperger, U., Lohmann, U., and
666   Cziczo, D. J.: In situ determination of atmospheric aerosol composition as a function of hygroscopic
667   growth, Journal of Geophysical Research: Atmospheres, 113, https://doi.org/10.1029/2008JD009954,
668   2008.

669   Herich, H., Kammermann, L., Friedman, B., Gross, D. S., Weingartner, E., Lohmann, U.,
670   Spichtinger, P., Gysel, M., Baltensperger, U., and Cziczo, D. J.: Subarctic atmospheric aerosol
671   composition: 2. Hygroscopic growth properties, Journal of Geophysical Research: Atmospheres, 114,
672   https://doi.org/10.1029/2008JD011574, 2009.

673   Hong, J., Äijälä, M., Häme, S. A. K., Hao, L., Duplissy, J., Heikkinen, L. M., Nie, W., Mikkilä,
674   J., Kulmala, M., Prisle, N. L., Virtanen, A., Ehn, M., Paasonen, P., Worsnop, D. R., Riipinen, I., Petäjä,
675   T., and Kerminen, V.-M.: Estimates of the organic aerosol volatility in a boreal forest using two
676   independent methods, Atmos. Chem. Phys., 17, 4387–4399, https://doi.org/10.5194/acp-17-4387-
677   2017, 2017.

678   Jayne, J. T., Leard, D. C., Zhang, X., Davidovits, P., Smith, K. A., Kolb, C. E., and Worsnop, D.
679   R.: Development of an Aerosol Mass Spectrometer for Size and Composition Analysis of Submicron
680   Particles, Aerosol Science and Technology, 33, 49–70, https://doi.org/10.1080/027868200410840,
681   2000.

682   Jiang, X., Tao, J., Kuang, Y., Hong, J., and Ma, N.: Mathematical derivation and physical
683   interpretation of particle size-resolved activation ratio based on particle hygroscopicity distribution:
684   Application on global characterization of CCN activity, Atmospheric Environment, 246, 118137,
685   https://doi.org/10.1016/j.atmosenv.2020.118137, 2021.

686   Jurányi, Z., Tritscher, T., Gysel, M., Laborde, M., Gomes, L., Roberts, G., Baltensperger, U., and
687   Weingartner, E.: Hygroscopic mixing state of urban aerosol derived from size-resolved cloud
688   condensation nuclei measurements during the MEGAPOLI campaign in Paris, Atmos. Chem. Phys.,
689   13, 6431–6446, https://doi.org/10.5194/acp-13-6431-2013, 2013.

690   Kawana, K., Nakayama, T., and Mochida, M.: Hygroscopicity and CCN activity of atmospheric
691   aerosol particles and their relation to organics: Characteristics of urban aerosols in Nagoya, Japan,
692   Journal   of   Geophysical   Research: Atmospheres,   121,   4100–4121,
693   https://doi.org/10.1002/2015jd023213, 2016.

694   Kim, N., Yum, S. S., Park, M., Park, J. S., Shin, H. J., and Ahn, J. Y.: Hygroscopicity of urban
695   aerosols and its link to size-resolved chemical composition during spring and summer in Seoul, Korea,
696   Atmos. Chem. Phys., 20, 11245–11262, https://doi.org/10.5194/acp-20-11245-2020, 2020.

697   Kuang, Y., Zhao, C. S., Tao, J. C., and Ma, N.: Diurnal variations of aerosol optical properties in
698   the North China Plain and their influences on the estimates of direct aerosol radiative effect, Atmos.
699   Chem. Phys., 15, 5761–5772, https://doi.org/10.5194/acp-15-5761-2015, 2015.

700   Kuang, Y., He, Y., Xu, W., Yuan, B., Zhang, G., Ma, Z., Wu, C., Wang, C., Wang, S., Zhang, S.,
701   Tao, J., Ma, N., Su, H., Cheng, Y., Shao, M., and Sun, Y.: Photochemical Aqueous-Phase Reactions

Induce Rapid Daytime Formation of Oxygenated Organic Aerosol on the North China Plain, Environmental Science & Technology, 54, 3849–3860, https://doi.org/10.1021/acs.est.9b06836, 2020.

Kuwata, M. and Kondo, Y.: Dependence of size-resolved CCN spectra on the mixing state of nonvolatile cores observed in Tokyo, Journal of Geophysical Research: Atmospheres, 113, https://doi.org/10.1029/2007JD009761, 2008.

Kuwata, M., Kondo, Y., Mochida, M., Takegawa, N., and Kawamura, K.: Dependence of CCN activity of less volatile particles on the amount of coating observed in Tokyo, Journal of Geophysical Research: Atmospheres, 112, https://doi.org/10.1029/2006JD007758, 2007.

Lack, D. A., Langridge, J. M., Bahreini, R., Cappa, C. D., Middlebrook, A. M., and Schwarz, J. P.: Brown carbon and internal mixing in biomass burning particles, Proceedings of the National Academy of Sciences, 109, 14802–14807, https://doi.org/10.1073/pnas.1206575109, 2012.

Lance, S., Nenes, A., Medina, J., and Smith, J. N.: Mapping the operation of the DMT continuous flow CCN counter, Aerosol science and technology, 40, 242–254, 2006.

Lance, S., Raatikainen, T., Onasch, T. B., Worsnop, D. R., Yu, X. Y., Alexander, M. L., Stolzenburg, M. R., McMurry, P. H., Smith, J. N., and Nenes, A.: Aerosol mixing state, hygroscopic growth and cloud activation efficiency during MIRAGE 2006, Atmos. Chem. Phys., 13, 5049–5062, https://doi.org/10.5194/acp-13-5049-2013, 2013.

Lata, N. N., Zhang, B., Schum, S., Mazzoleni, L., Brimberry, R., Marcus, M. A., Cantrell, W. H., Fialho, P., Mazzoleni, C., and China, S.: Aerosol Composition, Mixing State, and Phase State of Free Tropospheric Particles and Their Role in Ice Cloud Formation, ACS Earth Space Chem., 5, 3499–3510, https://doi.org/10.1021/acsearthspacechem.1c00315, 2021.

Lee, A. K. Y., Rivellini, L.-H., Chen, C.-L., Liu, J., Price, D. J., Betha, R., Russell, L. M., Zhang, X., and Cappa, C. D.: Influences of Primary Emission and Secondary Coating Formation on the Particle Diversity and Mixing State of Black Carbon Particles, Environ. Sci. Technol., 53, 9429–9438, https://doi.org/10.1021/acs.est.9b03064, 2019.

Li, G., Su, H., Ma, N., Tao, J., Kuang, Y., Wang, Q., Hong, J., Zhang, Y., Kuhn, U., and Zhang, S.: Multiphase chemistry experiment in Fogs and Aerosols in the North China Plain (McFAN): integrated analysis and intensive winter campaign 2018, Faraday Discussions, 2021.

Liu, D., Joshi, R., Wang, J., Yu, C., Allan, J. D., Coe, H., Flynn, M. J., Xie, C., Lee, J., Squires, F., Kotthaus, S., Grimmond, S., Ge, X., Sun, Y., and Fu, P.: Contrasting physical properties of black carbon in urban Beijing between winter and summer, Atmos. Chem. Phys., 19, 6749–6769, https://doi.org/10.5194/acp-19-6749-2019, 2019.

Liu, D., Li, S., Hu, D., Kong, S., Cheng, Y., Wu, Y., Ding, S., Hu, K., Zheng, S., Yan, Q., Zheng, H., Zhao, D., Tian, P., Ye, J., Huang, M., and Ding, D.: Evolution of Aerosol Optical Properties from Wood Smoke in Real Atmosphere Influenced by Burning Phase and Solar Radiation, Environ. Sci. Technol., 55, 5677–5688, https://doi.org/10.1021/acs.est.0c07569, 2021.

Liu, K., Zhang, C., Cheng, Y., Liu, C., Zhang, H., Zhang, G., Sun, X., and Mu, Y.: Serious BTEX pollution in rural area of the North China Plain during winter season, Journal of Environmental Sciences, 30, 186–190, https://doi.org/10.1016/j.jes.2014.05.056, 2015.

741   Liu, P. F., Zhao, C. S., Göbel, T., Hallbauer, E., Nowak, A., Ran, L., Xu, W. Y., Deng, Z. Z., Ma,
742   N., and Mildenberger, K.: Hygroscopic properties of aerosol particles at high relative humidity and
743   their diurnal variations in the North China Plain, Atmos. Chem. Phys, 11, 3479–3494, 2011.

744   Luo, B., Kuang, Y., Huang, S., Song, Q., Hu, W., Li, W., Peng, Y., Chen, D., Yue, D., Yuan, B.,
745   and Shao, M.: Parameterizations of size distribution and refractive index of biomass burning organic
746   aerosol with black carbon content, Atmos. Chem. Phys., 22, 12401–12415,
747   https://doi.org/10.5194/acp-22-12401-2022, 2022.

748   Ma, N., Zhao, C. S., Müller, T., Cheng, Y. F., Liu, P. F., Deng, Z. Z., Xu, W. Y., Ran, L., Nekat,
749   B., van Pinxteren, D., Gnauk, T., Müller, K., Herrmann, H., Yan, P., Zhou, X. J., and Wiedensohler,
750   A.: A new method to determine the mixing state of light absorbing carbonaceous using the measured
751   aerosol optical properties and number size distributions, Atmos. Chem. Phys., 12, 2381–2397,
752   https://doi.org/10.5194/acp-12-2381-2012, 2012.

753   Ma, N., Zhao, C., Tao, J., Wu, Z., Kecorius, S., Wang, Z., Größ, J., Liu, H., Bian, Y., Kuang, Y.,
754   Teich, M., Spindler, G., Müller, K., van Pinxteren, D., Herrmann, H., Hu, M., and Wiedensohler, A.:
755   Variation of CCN activity during new particle formation events in the North China Plain, Atmos. Chem.
756   Phys., 16, 8593–8607, https://doi.org/10.5194/acp-16-8593-2016, 2016.

757   Matsui, H., Hamilton, D. S., and Mahowald, N. M.: Black carbon radiative effects highly sensitive
758   to emitted particle size when resolving mixing-state diversity, Nature Communications, 9, 3446,
759   https://doi.org/10.1038/s41467-018-05635-1, 2018.

760   Mei, F., Hayes, P. L., Ortega, A., Taylor, J. W., Allan, J. D., Gilman, J., Kuster, W., de Gouw, J.,
761   Jimenez, J. L., and Wang, J.: Droplet activation properties of organic aerosols observed at an urban
762   site during CalNex-LA, Journal of Geophysical Research-Atmospheres, 118, 2903–2917,
763   https://doi.org/10.1002/jgrd.50285, 2013.

764   Metcalf, A. R., Craven, J. S., Ensberg, J. J., Brioude, J., Angevine, W., Sorooshian, A., Duong,
765   H. T., Jonsson, H. H., Flagan, R. C., and Seinfeld, J. H.: Black carbon aerosol over the Los Angeles
766   Basin during CalNex, Journal of Geophysical Research: Atmospheres, 117,
767   https://doi.org/10.1029/2011JD017255, 2012.

768   Middlebrook, A. M., Bahreini, R., Jimenez, J. L., and Canagaratna, M. R.: Evaluation of
769   Composition-Dependent Collection Efficiencies for the Aerodyne Aerosol Mass Spectrometer using
770   Field Data, Aerosol Science and Technology, 46, 258–271,
771   https://doi.org/10.1080/02786826.2011.620041, 2012.

772   Moffet, R. C., O'Brien, R. E., Alpert, P. A., Kelly, S. T., Pham, D. Q., Gilles, M. K., Knopf, D.
773   A., and Laskin, A.: Morphology and mixing of black carbon particles collected in central California
774   during the CARES field study, Atmos. Chem. Phys., 16, 14515–14525, https://doi.org/10.5194/acp-
775   16-14515-2016, 2016.

776   Mohr, C., Huffman, J. A., Cubison, M. J., Aiken, A. C., Docherty, K. S., Kimmel, J. R., Ulbrich,
777   I. M., Hannigan, M., and Jimenez, J. L.: Characterization of Primary Organic Aerosol Emissions from
778   Meat Cooking, Trash Burning, and Motor Vehicles with High-Resolution Aerosol Mass Spectrometry
779   and Comparison with Ambient and Chamber Observations, Environ. Sci. Technol., 43, 2443–2449,
780   https://doi.org/10.1021/es8011518, 2009.

781   Moteki, N. and Kondo, Y.: Effects of Mixing State on Black Carbon Measurements by Laser-
782   Induced   Incandescence,   Aerosol   Science   and   Technology,   41,   398–417,
783   https://doi.org/10.1080/02786820701199728, 2007.

784   Nordmann, S., Cheng, Y. F., Carmichael, G. R., Yu, M., Denier van der Gon, H. A. C., Zhang,
785   Q., Saide, P. E., Pöschl, U., Su, H., Birmili, W., and Wiedensohler, A.: Atmospheric black carbon and
786   warming effects influenced by the source and absorption enhancement in central Europe, Atmos. Chem.
787   Phys., 14, 12683–12699, https://doi.org/10.5194/acp-14-12683-2014, 2014.

788   Paatero, P. and Tapper, U.: Positive matrix factorization: A non-negative factor model with
789   optimal   utilization   of   error   estimates   of   data   values,   Environmetrics,   5,   111–126,
790   https://doi.org/10.1002/env.3170050203, 1994.

791   Peng, J., Hu, M., Guo, S., Du, Z., Zheng, J., Shang, D., Levy Zamora, M., Zeng, L., Shao, M.,
792   Wu, Y.-S., Zheng, J., Wang, Y., Glen, C. R., Collins, D. R., Molina, M. J., and Zhang, R.: Markedly
793   enhanced absorption and direct radiative forcing of black carbon under polluted urban environments,
794   Proceedings   of   the   National   Academy   of   Sciences,   113,   4266–4271,
795   https://doi.org/10.1073/pnas.1602310113, 2016.

796   Philippin, S., Wiedensohler, A., and Stratmann, F.: Measurements of non-volatile fractions of
797   pollution aerosols with an eight-tube volatility tandem differential mobility analyzer (VTDMA-8),
798   Journal of Aerosol Science, 35, 185–203, https://doi.org/10.1016/j.jaerosci.2003.07.004, 2004.

799   Ren, J., Zhang, F., Wang, Y., Collins, D., Fan, X., Jin, X., Xu, W., Sun, Y., Cribb, M., and Li, Z.:
800   Using different assumptions of aerosol mixing state and chemical composition to predict CCN
801   concentrations based on field measurements in urban Beijing, Atmospheric Chemistry and Physics,
802   18, 6907–6921, https://doi.org/10.5194/acp-18-6907-2018, 2018.

803   Riemer, N., Ault, A. P., West, M., Craig, R. L., and Curtis, J. H.: Aerosol Mixing State:
804   Measurements,   Modeling,   and   Impacts,   Reviews   of   Geophysics,   57,   187–249,
805   https://doi.org/10.1029/2018RG000615, 2019.

806   Roberts, G. C. and Nenes, A.: A continuous-flow streamwise thermal-gradient CCN chamber for
807   atmospheric measurements, Aerosol science and technology, 39, 206–221, 2005.

808   Rose, D., Gunthe, S. S., Mikhailov, E., Frank, G. P., Dusek, U., Andreae, M. O., and Pöschl, U.:
809   Calibration and measurement uncertainties of a continuous-flow cloud condensation nuclei counter
810   (DMT-CCNC): CCN activation of ammonium sulfate and sodium chloride aerosol particles in theory
811   and experiment, Atmos. Chem. Phys., 8, 1153–1179, 2008.

812   Rose, D., Nowak, A., Achtert, P., Wiedensohler, A., Hu, M., Shao, M., Zhang, Y., Andreae, M.
813   O., and Poschl, U.: Cloud condensation nuclei in polluted air and biomass burning smoke near the
814   mega-city Guangzhou, China - Part 1: Size-resolved measurements and implications for the modeling
815   of aerosol particle hygroscopicity and CCN activity, Atmos. Chem. Phys., 10, 3365–3383, 2010.

816   Rose, D., Gunthe, S. S., Su, H., Garland, R. M., Yang, H., Berghof, M., Cheng, Y. F., Wehner,
817   B., Achtert, P., Nowak, A., Wiedensohler, A., Takegawa, N., Kondo, Y., Hu, M., Zhang, Y., Andreae,
818   M. O., and Poschl, U.: Cloud condensation nuclei in polluted air and biomass burning smoke near the
819   mega-city Guangzhou, China -Part 2: Size-resolved aerosol chemical composition, diurnal cycles, and

Atmospheric
Chemistry
and Physics
Discussions

externally mixed weakly CCN-active soot particles, Atmos. Chem. Phys., 11, 2817–2836, https://doi.org/10.5194/acp-11-2817-2011, 2011.

Saha, P. K., Khlystov, A., and Grieshop, A. P.: Downwind evolution of the volatility and mixing state of near-road aerosols near a US interstate highway, Atmos. Chem. Phys., 18, 2139–2154, https://doi.org/10.5194/acp-18-2139-2018, 2018.

Sedlacek, A. J., Lewis, E. R., Kleinman, L., Xu, J., and Zhang, Q.: Determination of and evidence for non-core-shell structure of particles containing black carbon using the Single-Particle Soot Photometer (SP2), Geophysical Research Letters, 39, L06802, https://doi.org/10.1029/2012GL050905, 2012.

Shi, J., Hong, J., Ma, N., Luo, Q., He, Y., Xu, H., Tan, H., Wang, Q., Tao, J., Zhou, Y., Han, S., Peng, L., Xie, L., Zhou, G., Xu, W., Sun, Y., Cheng, Y., and Su, H.: Measurement report: On the difference in aerosol hygroscopicity between high and low relative humidity conditions in the North China Plain, Atmos. Chem. Phys., 22, 4599–4613, https://doi.org/10.5194/acp-22-4599-2022, 2022.

Stevens, R., Ryjkov, A., Majdzadeh, M., and Dastoor, A.: An improved representation of aerosol mixing state for air quality–weather interactions, Atmos. Chem. Phys., 22, 13527–13549, https://doi.org/10.5194/acp-22-13527-2022, 2022.

Stolzenburg, M. R. and McMurry, P. H.: Equations governing single and tandem DMA configurations and a new lognormal approximation to the transfer function, Aerosol Science and Technology, 42, 421–432, 2008.

Su, H., Rose, D., Cheng, Y. F., Gunthe, S. S., Massling, A., Stock, M., Wiedensohler, A., Andreae, M. O., and Poschl, U.: Hygroscopicity distribution concept for measurement data analysis and modeling of aerosol particle mixing state with regard to hygroscopic growth and CCN activation, Atmos. Chem. Phys., 10, 7489–7503, https://doi.org/10.5194/acp-10-7489-2010, 2010.

Subramanian, R., Kok, G. L., Baumgardner, D., Clarke, A., Shinozuka, Y., Campos, T. L., Heizer, C. G., Stephens, B. B., de Foy, B., Voss, P. B., and Zaveri, R. A.: Black carbon over Mexico: the effect of atmospheric transport on mixing state, mass absorption cross-section, and BC/CO ratios, Atmos. Chem. Phys., 10, 219–237, https://doi.org/10.5194/acp-10-219-2010, 2010.

Tan, H., Xu, H., Wan, Q., Li, F., Deng, X., Chan, P. W., Xia, D., and Yin, Y.: Design and Application of an Unattended Multifunctional H-TDMA System, Journal of Atmospheric and Oceanic Technology, 30, 1136–1148, https://doi.org/10.1175/JTECH-D-12-00129.1, 2013.

Tao, J., Zhao, C., Nan, M., and Ye, K.: Consistency and applicability of parameterization schemes for the size-resolved aerosol activation ratio based on field measurements in the North China Plain, Atmospheric Environment, 173, 316–324, 2018.

Tao, J., Kuang, Y., Ma, N., Zheng, Y., Wiedensohler, A., and Zhao, C.: An improved parameterization scheme for size-resolved particle activation ratio and its application on comparison study of particle hygroscopicity measurements between HTDMA and DMA-CCNC, Atmospheric Environment, 226, 117403, https://doi.org/10.1016/j.atmosenv.2020.117403, 2020.

Tao, J., Kuang, Y., Ma, N., Hong, J., Sun, Y., Xu, W., Zhang, Y., He, Y., Luo, Q., Xie, L., Su, H., and Cheng, Y.: Secondary aerosol formation alters CCN activity in the North China Plain, Atmos. Chem. Phys., 21, 7409–7427, https://doi.org/10.5194/acp-21-7409-2021, 2021.

Atmospheric
Chemistry
and Physics
Discussions

860   Tao, M., Chen, L., Su, L., and Tao, J.: Satellite observation of regional haze pollution over the
861   North China Plain, Journal of Geophysical Research: Atmospheres, 117,
862   https://doi.org/10.1029/2012JD017915, 2012.

863   Thalman, R., de Sa, S. S., Palm, B. B., Barbosa, H. M. J., Poehlker, M. L., Alexander, M. L.,
864   Brito, J., Carbone, S., Castillo, P., Day, D. A., Kuang, C., Manzi, A., Ng, N. L., Sedlacek, A. J., Souza,
865   R., Springston, S., Watson, T., Poehlker, C., Poeschl, U., Andreae, M. O., Artaxo, P., Jimenez, J. L.,
866   Martin, S. T., and Wang, J.: CCN activity and organic hygroscopicity of aerosols downwind of an
867   urban region in central Amazonia: seasonal and diel variations and impact of anthropogenic emissions,
868   Atmospheric Chemistry and Physics, 17, 11779–11801, https://doi.org/10.5194/acp-17-11779-2017,
869   2017.

870   Ting, Y., Mitchell, E. J. S., Allan, J. D., Liu, D., Spracklen, D. V., Williams, A., Jones, J. M.,
871   Lea-Langton, A. R., McFiggans, G., and Coe, H.: Mixing State of Carbonaceous Aerosols of Primary
872   Emissions from "Improved" African Cookstoves, Environ. Sci. Technol., 52, 10134–10143,
873   https://doi.org/10.1021/acs.est.8b00456, 2018.

874   Tomlin, J. M., Jankowski, K. A., Veghte, D. P., China, S., Wang, P., Fraund, M., Weis, J., Zheng,
875   G., Wang, Y., Rivera-Adorno, F., Raveh-Rubin, S., Knopf, D. A., Wang, J., Gilles, M. K., Moffet, R.
876   C., and Laskin, A.: Impact of dry intrusion events on the composition and mixing state of particles
877   during the winter Aerosol and Cloud Experiment in the Eastern North Atlantic (ACE-ENA), Atmos.
878   Chem. Phys., 21, 18123–18146, https://doi.org/10.5194/acp-21-18123-2021, 2021.

879   Ulbrich, I. M., Canagaratna, M. R., Zhang, Q., Worsnop, D. R., and Jimenez, J. L.: Interpretation
880   of organic components from Positive Matrix Factorization of aerosol mass spectrometric data, Atmos.
881   Chem. Phys., 9, 2891–2918, https://doi.org/10.5194/acp-9-2891-2009, 2009.

882   Wang, X., Ye, X., Chen, J., Wang, X., Yang, X., Fu, T.-M., Zhu, L., and Liu, C.: Direct links
883   between hygroscopicity and mixing state of ambient aerosols: estimating particle hygroscopicity from
884   their single-particle mass spectra, Atmos. Chem. Phys., 20, 6273–6290, https://doi.org/10.5194/acp-
885   20-6273-2020, 2020.

886   Wang, Y., Wang, X., Kondo, Y., Kajino, M., Munger, J. W., and Hao, J.: Black carbon and its
887   correlation with trace gases at a rural site in Beijing: Top-down constraints from ambient
888   measurements on bottom-up emissions, Journal of Geophysical Research: Atmospheres, 116,
889   https://doi.org/10.1029/2011JD016575, 2011.

890   Wang, Y., Zhang, F., Li, Z., Tan, H., Xu, H., Ren, J., Zhao, J., Du, W., and Sun, Y.: Enhanced
891   hydrophobicity and volatility of submicron aerosols under severe emission control conditions in
892   Beijing, Atmos. Chem. Phys., 17, 5239–5251, https://doi.org/10.5194/acp-17-5239-2017, 2017.

893   Wang, Y., Hu, R., Wang, Q., Li, Z., Cribb, M., Sun, Y., Song, X., Shang, Y., Wu, Y., Huang, X.,
894   and Wang, Y.: Different effects of anthropogenic emissions and aging processes on the mixing state
895   of soot particles in the nucleation and accumulation modes, Atmos. Chem. Phys., 22, 14133–14146,
896   https://doi.org/10.5194/acp-22-14133-2022, 2022.

897   Wehner, B., Berghof, M., Cheng, Y. F., Achtert, P., Birmili, W., Nowak, A., Wiedensohler, A.,
898   Garland, R. M., Pöschl, U., Hu, M., and Zhu, T.: Mixing state of nonvolatile aerosol particle fractions
899   and comparison with light absorption in the polluted Beijing region, Journal of Geophysical Research:
900   Atmospheres, 114, https://doi.org/10.1029/2008JD010923, 2009.

901 Wu, Y., Wang, X., Tao, J., Huang, R., Tian, P., Cao, J., Zhang, L., Ho, K.-F., Han, Z., and Zhang,
902 R.: Size distribution and source of black carbon aerosol in urban Beijing during winter haze episodes,
903 Atmos. Chem. Phys., 17, 7965–7975, https://doi.org/10.5194/acp-17-7965-2017, 2017.

904 Xu, W., Sun, Y., Wang, Q., Zhao, J., Wang, J., Ge, X., Xie, C., Zhou, W., Du, W., Li, J., Fu, P.,
905 Wang, Z., Worsnop, D. R., and Coe, H.: Changes in Aerosol Chemistry From 2014 to 2016 in Winter
906 in Beijing: Insights From High-Resolution Aerosol Mass Spectrometry, Journal of Geophysical
907 Research: Atmospheres, 124, 1132–1147, https://doi.org/10.1029/2018JD029245, 2019.

908 Xu, W. Y., Zhao, C. S., Ran, L., Deng, Z. Z., Liu, P. F., Ma, N., Lin, W. L., Xu, X. B., Yan, P.,
909 He, X., Yu, J., Liang, W. D., and Chen, L. L.: Characteristics of pollutants and their correlation to
910 meteorological conditions at a suburban site in the North China Plain, Atmos. Chem. Phys., 11, 4353–
911 4369, https://doi.org/10.5194/acp-11-4353-2011, 2011.

912 Yang, Z., Ma, N., Wang, Q., Li, G., Pan, X., Dong, W., Zhu, S., Zhang, S., Gao, W., He, Y., Xie,
913 L., Zhang, Y., Kuhn, U., Xu, W., Kuang, Y., Tao, J., Hong, J., Zhou, G., Sun, Y., Su, H., and Cheng,
914 Y.: Characteristics and source apportionment of black carbon aerosol in the North China Plain,
915 Atmospheric Research, 276, 106246, https://doi.org/10.1016/j.atmosres.2022.106246, 2022.

916 Zhang, F., Li, Y., Li, Z., Sun, L., Li, R., Zhao, C., Wang, P., Sun, Y., Liu, X., Li, J., Li, P., Ren,
917 G., and Fan, T.: Aerosol hygroscopicity and cloud condensation nuclei activity during the AC3Exp
918 campaign: implications for cloud condensation nuclei parameterization, Atmos. Chem. Phys., 14,
919 13423–13437, https://doi.org/10.5194/acp-14-13423-2014, 2014.

920 Zhang, S., Shen, X., Sun, J., Zhang, Y., Zhang, X., Xia, C., Hu, X., Zhong, J., Wang, J., and Liu,
921 S.: Atmospheric Particle Hygroscopicity and the Influence by Oxidation State of Organic Aerosols in
922 Urban Beijing, Journal of Environmental Sciences, 124, 544–556,
923 https://doi.org/10.1016/j.jes.2021.11.019, 2023.

924 Zhang, S. L., Ma, N., Kecorius, S., Wang, P. C., Hu, M., Wang, Z. B., Größ, J., Wu, Z. J., and
925 Wiedensohler, A.: Mixing state of atmospheric particles over the North China Plain, Atmospheric
926 Environment, 125, 152–164, 2016.

927 Zhao, G., Tao, J., Kuang, Y., Shen, C., Yu, Y., and Zhao, C.: Role of black carbon mass size
928 distribution in the direct aerosol radiative forcing, Atmos. Chem. Phys., 19, 13175–13188,
929 https://doi.org/10.5194/acp-19-13175-2019, 2019.

930 Zhao, G., Tan, T., Hu, S., Du, Z., Shang, D., Wu, Z., Guo, S., Zheng, J., Zhu, W., Li, M., Zeng,
931 L., and Hu, M.: Mixing state of black carbon at different atmospheres in north and southwest China,
932 Atmos. Chem. Phys., 22, 10861–10873, https://doi.org/10.5194/acp-22-10861-2022, 2022.

933 Zheng, H., Kong, S., Wu, F., Cheng, Y., Niu, Z., Zheng, S., Yang, G., Yao, L., Yan, Q., Wu, J.,
934 Zheng, M., Chen, N., Xu, K., Yan, Y., Liu, D., Zhao, D., Zhao, T., Bai, Y., Li, S., and Qi, S.: Intra-
935 regional transport of black carbon between the south edge of the North China Plain and central China
936 during winter haze episodes, Atmos. Chem. Phys., 19, 4499–4516, https://doi.org/10.5194/acp-19-
937 4499-2019, 2019.

938 Zhuang, B. L., Li, S., Wang, T. J., Deng, J. J., Xie, M., Yin, C. Q., and Zhu, J. L.: Direct radiative
939 forcing and climate effects of anthropogenic aerosols with different mixing states over China,
940 Atmospheric Environment, 79, 349–361, https://doi.org/10.1016/j.atmosenv.2013.07.004, 2013.